

# QUIET SUN MAGNETIC FIELDS FROM SIMULTANEOUS INVERSIONS OF VISIBLE AND INFRARED SPECTROPOLARIMETRIC OBSERVATIONS

I. DOMÍNGUEZ CERDEÑA

Instituto de Astrofísica de Canarias, E-38205 La Laguna, Spain

J. SÁNCHEZ ALMEIDA

Instituto de Astrofísica de Canarias, E-38205 La Laguna, Spain

AND

F. KNEER

Institut für Astrophysik, Friedrich-Hund-Platz 1, D-37077 Göttingen, Germany

(Dated: )

Draft version May 13, 2018

## ABSTRACT

We study the quiet Sun magnetic fields using spectropolarimetric observations of the infrared and visible Fe I lines at 6301.5, 6302.5, 15648 and 15653 Å. Magnetic field strengths and filling factors are inferred by the simultaneous fit of the observed Stokes profiles under the MISMA hypothesis. The observations cover an intra-network region at the solar disk center. We analyze 2280 Stokes profiles whose polarization signals are above noise in the two spectral ranges, which correspond to 40% of the field of view. Most of these profiles can be reproduced only with a model atmosphere including 3 magnetic components with very different field strengths, which indicates the co-existence of kG and sub-kG fields in our 1''5 resolution elements. We measure an unsigned magnetic flux density of 9.6 G considering the full field of view. Half of the pixels present magnetic fields with mixed polarities in the resolution element. The fraction of mixed polarities increases as the polarization weakens. We compute the probability density function of finding each magnetic field strength. It has a significant contribution of kG field strengths, which concentrates most of the observed magnetic flux and energy. This kG contribution has a preferred magnetic polarity, while the polarity of the weak fields is balanced.

*Subject headings:* Sun: magnetic fields – Sun: photosphere

## 1. INTRODUCTION

The quiet Sun can be defined as that part of the Sun far from magnetic activity. If we exclude plages and network, the remaining quiet area covers 90% of the surface of the Sun, and remains almost unchanged during the solar cycle (e.g., Harvey-Angle 1993). Few decades ago, this internetwork (IN) was thought to be almost devoid of magnetic fields and consequently, its relevance for the solar magnetism was not obvious (Livingston & Harvey 1975; Smithson 1975). However, with the present instrumentation, when the spatial resolution is around 1'', the quiet Sun turns out to be full of magnetic fields (Grossmann-Doerth et al. 1996; Lin & Rimmele 1999; Sánchez Almeida & Lites 2000), with an unsigned flux density measured with techniques based on the Zeeman effect of the order of 10 G (e.g., Sánchez Almeida & Lites 2000; Lites 2002). The analysis of observations with a spatial resolution twice better yields an unsigned flux twice larger (Domínguez Cerdeña et al. 2003a)<sup>1</sup>. There are reasons to believe that these resolutions are not enough to completely resolve the magnetic structures (see Sánchez Almeida et al. 2003b, and references therein). Recent measurements based on the Hanle effect find an unsigned flux of, at least, 60 G (Trujillo Bueno et al. 2004; Bommier et al. 2005), which is much higher than the magnetic flux observed with Zeeman techniques. Considering the fraction of solar surface corre-

sponding to the quiet Sun, the flux measured in the IN is comparable to (or larger than) that coming from all active regions even in the maximum of activity. Thus, the quiet Sun may play a significant role in the physical processes governing the solar global magnetism (e.g., Unno 1959; Stenflo 1982; Sánchez Almeida 2003a; Schrijver & Title 2003).

The topology and the scale of variation of the quiet Sun magnetic fields are not yet clear. There is evidence for the existence of mixed polarities, at least when the spatial resolution is 1'' (Sánchez Almeida et al. 1996; Sigwarth et al. 1999; Sánchez Almeida & Lites 2000; Lites 2002; Khomenko et al. 2003). The small-scale magnetic structures in the quiet Sun seem to be smaller than 50–100 km (see Khomenko et al. 2003; Domínguez Cerdeña et al. 2003b). This size assumes one single structure in the resolution element, however, it is to be expected that the dynamical influence of the granulation on the magnetic fields produces a distribution of many smaller structures. This fragmentation shows up in MHD simulations of turbulent dynamos (Cattaneo 1999; Emonet & Cattaneo 2001), and 3D magneto-convection (e.g., Stein & Nordlund 2002; Vögler 2003; Vögler et al. 2005). Recently, Cameron & Galloway (2005) studied various mechanisms proposed to produce intense magnetic concentrations and limited the radii of the magnetic flux tubes to less than 10 km, which is approximately the magnetic diffusion length scale (Schüssler 1986). This scenario was already proposed by Sánchez Almeida et al. (1996) with an atmosphere formed by optically thin magnetic structures with diverse properties (see also Sánchez Almeida 1998). Such a scheme is called MISMA (Micro-Structured Magnetized Atmosphere).

Electronic address: itahiza@iac.es

Electronic address: jos@iac.es

Electronic address: kneer@astro.physik.uni-goettingen.de

<sup>1</sup> However, see Lites & Socas-Navarro (2004).

An inversion procedure based on it has been able to fit the whole variety of asymmetric Stokes profiles<sup>2</sup> produced by the quiet Sun magnetic fields (Sánchez Almeida & Lites 2000; Socas-Navarro & Sánchez Almeida 2002).

Observational studies based on infrared (IR) spectral lines find magnetic field strengths in the range below 1 kG (sub-kG; Lin & Rimmele 1999; Khomenko et al. 2003), while works using lines in the visible spectral range tend to find kG fields (Grossmann-Doerth et al. 1996; Sigwarth et al. 1999; Sánchez Almeida & Lites 2000; Socas-Navarro & Sánchez Almeida 2002; Domínguez Cerdeña et al. 2003a,b; Lites & Socas-Navarro 2004). Kilogauss fields are also inferred from the presence of a considerable number of G-band bright points in the quiet Sun (Sánchez Almeida et al. 2004; de Wijn et al. 2005). Sánchez Almeida & Lites (2000) put forward a solution for this apparent contradiction: the co-existence in the resolution element of a distribution of field strengths going from zero to kG. They show how to reproduce the observed bias with the vertical gradient of the field strength induced by the hydrostatic equilibrium in the atmosphere. Another possibility with the same consequences is a horizontal gradient (Socas-Navarro & Sánchez Almeida 2003). The presence of a range of field strengths from sub-kG to kG fields bias the measurements based on IR Stokes profiles to sub-kG fields. Such a particular behavior is due to the high sensitivity of the IR lines to magnetic fields. The Fe I  $\lambda 15648$  Å (used by Lin & Rimmele 1999; Khomenko et al. 2003) is magnetically saturated<sup>3</sup> at 400 G while the visible pair Fe I  $\lambda 6301.5$  Å, Fe I  $\lambda 6302.5$  Å (e.g., used by Sánchez Almeida & Lites 2000; Domínguez Cerdeña et al. 2003a) saturates at 1.5 kG. The IR polarization signals coming from the strongest fields are spread in a wide range of wavelengths and they produce little signal. On the contrary, weak fields saturate the IR line and a significant Stokes V signal is built up in a narrow wavelength range. Weak field and strong field components appear in the same wavelengths in the visible lines so that their relative contribution is proportional to their magnetic flux. The weak field component can dominate over the strong component in the IR Stokes V profiles, while the strong fields dominate over the weak ones in the visible profiles. Thus, an incomplete analysis of the IR profiles leads to weak fields, whereas the same analysis of the visible lines shows strong fields. In order to test this conjecture, Sánchez Almeida et al. (2003a) presented simultaneous spectropolarimetric observations in the visible and IR ranges. An independent Milne-Eddington inversion of the visible and IR lines suggests the co-existence of sub-kG and kG fields. However, a more sophisticated and simultaneous inversion is desirable to provide further support to the conjecture of Sánchez Almeida & Lites (2000) and Socas-Navarro & Sánchez Almeida (2003).

This paper presents such simultaneous inversions under the MISMA approximation of the visible and the infrared Stokes profiles used in Sánchez Almeida et al. (2003a). As we discuss above, it seems to be appropriate for reproducing the

<sup>2</sup> We use the standard Stokes parameters to define the polarization state:  $I$  for the intensity,  $Q$  and  $U$  for the two orthonormal states of lineal polarization and  $V$  for the circular polarization. The Stokes profiles of a spectral line give the variation with wavelength of these four parameters. If the spectral line is formed in a homogeneous atmosphere, the Stokes profiles are expected to be symmetric or antisymmetric (e.g., Landi Degl'Innocenti 1992).

<sup>3</sup> The Stokes  $V$  signals no longer have a linear relationship with the magnetic field strength. The level of polarization stays constant while the splitting of the Stokes  $V$  lobes grows in proportion to the field strength.

TABLE 1  
ATOMIC PARAMETERS OF THE LINES UNDER STUDY.

Wavelength [Å]	$\chi$ [eV] <sup>a</sup>	$Agf$ <sup>b</sup>	Transition <sup>c</sup>	$g_L$
6301.499 <sup>d</sup>	3.65	$9.766 \cdot 10^{-6}$	$^5P_2 \ ^5D_2$	1.67
6302.492 <sup>d</sup>	3.69	$2.630 \cdot 10^{-6}$	$^5P_1 \ ^5D_0$	2.5
15648.515 <sup>e</sup>	5.426	$8.035 \cdot 10^{-6}$	$^7D_1 \ ^7D_1$	3
15652.874 <sup>e</sup>	6.246	$3.443 \cdot 10^{-5}$	$^7D_5 \ ^7D_4$	1.53

<sup>a</sup>Excitation potential from Moore et al. (1966) and Kurucz (1994).

<sup>b</sup>Abundance of Fe times statistical weight of the lower level times oscillator strength from Gurtovenko & Kostik (1981, visible lines) and from Borrero et al. (2003, IR lines).

<sup>c</sup>Spectral terms from Nave et al. (1994).

<sup>d</sup>Wavelengths from Higgs (1962).

<sup>e</sup>Wavelengths from Nave et al. (1994).

complex Stokes profiles produced by the quiet Sun. Section 2 summarizes the observations and the data reduction. Some properties of interest of the magnetograms obtained in the two spectral ranges are shown in § 3. The strategies for the data analysis and the inversion are explained in § 4. We present the results in § 5 whose consistency is analyzed in § 6. A final § 7 discusses the main conclusions.

## 2. OBSERVATIONS AND DATA REDUCTION

We re-analyze the spectra used by Sánchez Almeida et al. (2003a) whose properties are only sketched in the original reference. For the sake of comprehensiveness, the data and reduction are detailed here. The part of the reduction in which we bring the visible and IR spectra to equal spatial resolution is new.

We use two telescopes for the simultaneous visible and IR observation<sup>4</sup>. The observation was performed at the Spanish Observatorio del Teide (Tenerife, Spain). The IR spectra were gathered with the Tenerife Infrared Polarimeter (TIP, Collados 1999; Martínez Pillet et al. 1999) operated at the German Vacuum Tower Telescope (VTT). Spectrograms of the full Stokes vector ( $I, Q, U, V$ ) were obtained in the IR iron lines Fe I  $\lambda 15648$  Å (Landé factor  $g_L=3$ ) and Fe I  $\lambda 15652$  Å ( $g_L=1.53$ ). The visible observations were carried out with the French-Italian telescope THEMIS (Télescope Héliographique pour l'Étude du Magnétisme et des Instabilités Solaires) using the spectropolarimetric mode MTR (Mein & Rayrole 1985; Rayrole & Mein 1993). The lines analyzed are the pair Fe I  $\lambda 6301.5$  Å ( $g_L=1.66$ ) and Fe I  $\lambda 6302.5$  Å ( $g_L=2.5$ ). The atomic parameters of the four spectral lines are listed in Table 1. In order to obtain spectra in a two-dimensional field of view (FOV), the solar surface was scanned from East to West with a step size of 0''.5. The slit width was set to 0''.5 in both telescopes and the scan consisted in 60 positions. To improve the signal to noise ratio, the integration time was set to 30 s per position.

This work analyzes data obtained on August 10 2002 in a quiet Sun region close to disk center ( $\mu = 0.94$ ). We choose a region without magnetic activity as judged with the help of Ca II K and H $\alpha$  slit-jaw images from video cameras at the VTT. A video link between both telescopes providing the slit-jaw images from VTT at THEMIS was helpful to point both

<sup>4</sup> Nowadays, the observation is possible using a single telescope with TIP+POLIS (VTT, Tenerife, see Khomenko et al. 2005) and with SPINOR (DST, Sacramento Peak Observatory, see Socas-Navarro et al. 2005).

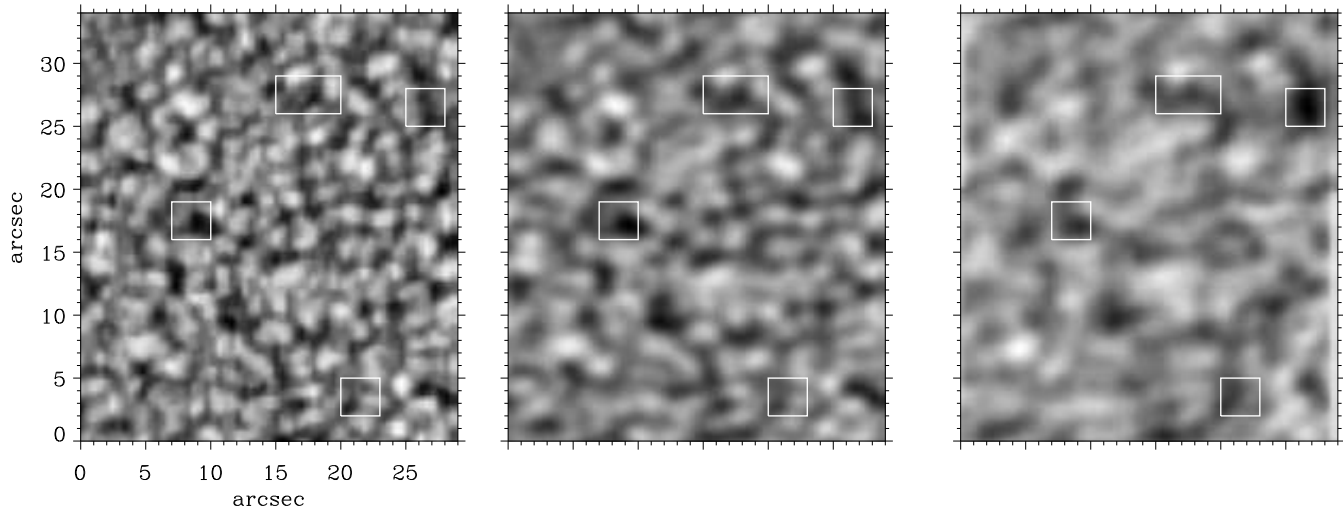


FIG. 1.— Intensity images in the continuum of the IR lines before (left) and after (middle) smearing, and continuum image of the visible lines (right). The rectangles point out structures that can be easily identified in both the IR and the visible images. Axes are in arcsec from the lower left corner.

telescopes to the same target. Since the absolute pointing of the telescopes was not accurate enough, and the slit-jaw images of the granulation did not allow us to recognize the region pointed by the two telescopes, we used another *differential* method for accurate pointing. First, both telescopes were pointed to a characteristic small structure which could easily be identified, e.g., a small pore. The pointing of the VTT was moved to a quiet Sun region, and then THEMIS pointing was displaced by the same distance. As we explain below, the scans provided by the VTT and THEMIS are post-processed for fine-tuning co-alignment. This final step removes residual pointing errors plus some additional effects (e.g., differential refraction between the visible and the IR). The scan under study here has an offset between telescopes of only  $1''$  (see below). Since we scanned with a step size of  $0''.5$  and with an exposure time of 30 s per step, the time lag between IR and visible data of the same point corresponds to only 1 minute.

The data reduction of the two data sets was carried out in a similar way. A flat-field correction was applied to the spectra. In order to get the Stokes parameters, we demodulate the measurements with the calibration matrix, and finally we correct for seeing-induced crosstalk by combining the two beams of each polarimeter. The crosstalk produced by instrumental polarization (IP) of the telescopes themselves was considered too. Since THEMIS is free of IP, the visible data do not need correction. Due to the configuration of mirrors in the VTT, the IR data are affected by an important crosstalk between the different Stokes parameters. It was calibrated with a model Mueller matrix set using a linear polarizer mounted at the entrance window of the telescope (see Collados 2003).

Since the purpose of this work is the simultaneous inversion of visible and IR lines, one needs a consistent scale of wavelengths in both spectral ranges. We carried out an absolute wavelength calibration so that the lines are unshifted in this scale when the solar plasma is at rest. The central wavelength of Fe I  $\lambda 6301.5$  Å and Fe I  $\lambda 6302.5$  Å was considered to be the zero-crossing of the Stokes  $V$  profiles corresponding to the signals in the network points of our FOV. Such a reference gives an accuracy of  $200 \text{ m s}^{-1}$  (Solanki 1986). Solanki & Stenflo (1986) find that the zero-crossing wave-

TABLE 2  
CONVECTIVE BLUE SHIFT OF THE SPECTRAL LINES.

line	$v_{CB}^a$ [ $\text{m s}^{-1}$ ]	$v_{CB}^b$ [ $\text{m s}^{-1}$ ]
Fe I $\lambda 6301.5$ Å	+50	-100
Fe I $\lambda 6302.5$ Å	-80	-150
Fe I $\lambda 15648$ Å	-370	-400
Fe I $\lambda 15652$ Å	-430	-400

<sup>a</sup>From synthesis in numerical simulations by (Asplund et al. 2000).

<sup>b</sup>From two-component inversion of many iron lines (Borrero & Bellot Rubio 2002; Borrero et al. 2003).

length depends on the spectral resolution. Using their simulations, we check that our resolution of  $21.9 \text{ mÅ}$  per pixel does not threaten the absolute accuracy given above. The strongest polarization signals were chosen to trace the network ( $V > 0.02 I_c$  with  $I_c$  the intensity of the continuum near the lines). Weaker signals tend to be red-shifted. Since this method has not been tested for the IR lines, their absolute wavelengths need another way of calibration. We computed the mean line profile from the data and then corrected for the expected convective blue-shift. We average the Stokes  $I$  profile over the FOV. The minima of the lines were fitted with fourth order polynomials whose minima were taken as the central wavelengths of the spectral lines. These wavelengths corrected for the convective blue-shifts provide the reference for an atmosphere at rest. Table 2 presents the convective blue-shift for Fe I  $\lambda 15648$  Å and Fe I  $\lambda 15652$  Å obtained from a two-component inversion of many line profiles in the quiet Sun (Borrero et al. 2003) and from line synthesis from numerical simulations of granulation (Asplund et al. 2000, private communication). We cannot assess the accuracy of our absolute wavelength calibration based on them, however, the fact that the two numerical simulations provide the same convective blue-shift suggests the consistency of the approach.

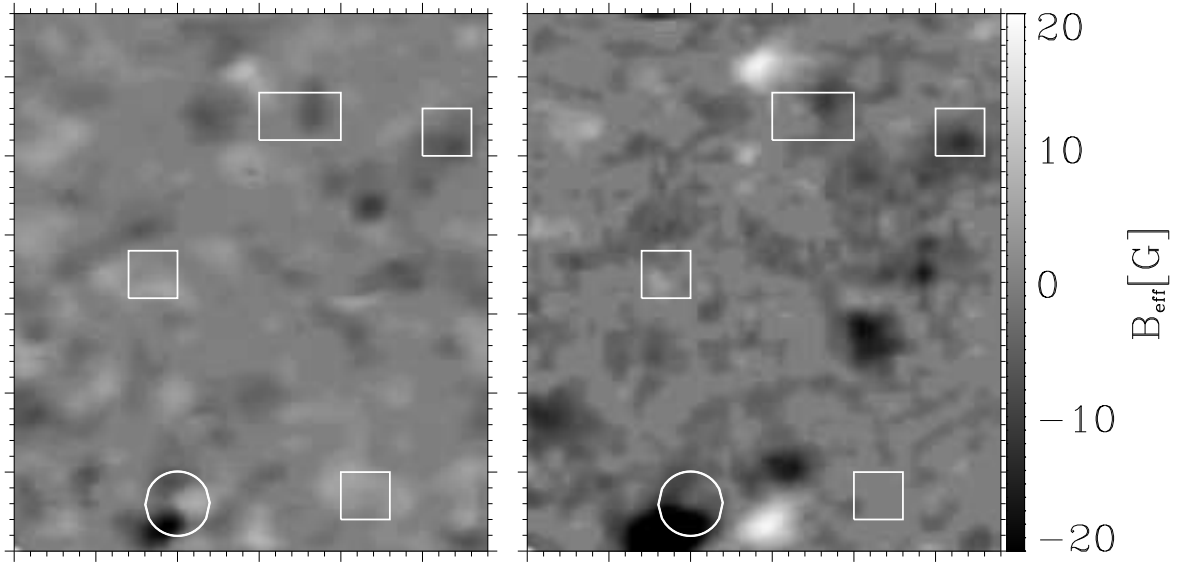


FIG. 2.— Magnetograms from Fe I  $\lambda 15648$  Å (left) and Fe I  $\lambda 6302.5$  Å (right). White and black distinguish the two polarities. Both magnetograms are scaled to flux densities  $|B_{\text{eff}}| < 20$  G. The distance between small tickmarks is  $1''$ .

One of the most important steps in the data reduction is the spatial co-alignment of the visible and IR scans. The aim of this process is to ensure that the scans are not only taken from the same region on the Sun but also that each individual pixel of the visible and IR scans come from the same point of the IN region. The correct alignment must be guaranteed for a meaningful analysis of the data, i.e., for the simultaneous interpretation of both data sets. In order to align the scans we displace and re-scale them allowing for five degrees of freedom. First, we correct for differences in the spatial scales along the  $X$  and  $Y$  directions. We define  $X$  as the direction of scanning and  $Y$  as the direction along the slit. The step width of the scans was slightly different in both telescopes (less than 1%), and the spatial scales along the slit were computed from the focal length of the telescopes. Their (relative) agreement with respect to each other were checked using reference images of a sunspot. Then, we found the shift in the  $X$  and  $Y$  directions by cross-correlation of the visible and IR continuum images. It corresponds to the offset of  $1''$  mentioned above. Finally both slits were not exactly oriented with the same angle with respect to the Sun. There was a small rotation of  $1^\circ$  which we also determine by cross-correlation. Once the correspondence between the visible and IR spatial coordinates was set, we interpolate the visible spectra to obtain the spectra at the positions of the pixels in the IR scan.

It is important to have the same spatial resolution in both data sets. However, the angular resolution of the observations at the VTT was better than at THEMIS due to the use of a correlation tracker (Ballesteros et al. 1996). To solve this problem, the IR data were degraded to the resolution of the visible data by convolution with a Gaussian. The contrast of the IR continuum image depends on the angular resolution. We set the width of the Gaussian, and so the angular

resolution of the IR map, by comparison with the synthetic images from numerical simulations of magneto-convection (Vögler 2003; Vögler et al. 2005). Specifically, we tune the IR contrast so that the ratio between the visible and the IR contrasts agrees with the ratio obtained from numerical simulations (0.48). Such theoretical ratio was found to be almost independent of the angular resolution and in excellent agreement with the value measured by Khomenko et al. (2005) using a single telescope to obtain simultaneous visible and IR data. The central panel in Figure 1 shows the continuum image in the IR after smearing. The contrast of the IR image is 0.9%. The right panel of Figure 1 contains the continuum intensity image of the visible data (contrast 1.9%). The squares point out regions easy to identify in both images showing the goodness of the alignment.

After all data reduction, including smearing of the IR data and Fourier filtering of the visible data, the level of noise in polarization for Stokes  $V$  is  $(2-3) \times 10^{-4} I_c$  for the IR data and  $5 \times 10^{-4} I_c$  for the visible data. A more detailed description of the telescopes and the data reduction can be found in Domínguez Cerdeña (2004). Descriptions of the instruments can be found in Collados (1999) and Schlichenmaier & Collados (2002) for TIP, and in López Ariste et al. (2000) and Bommier & Rayrole (2002) for THEMIS.

### 3. MAGNETOGRAMS

Figure 2 shows the magnetograms calculated from the Stokes  $V$  profiles of Fe I  $\lambda 6302.5$  Å and Fe I  $\lambda 15648$  Å. The longitudinal magnetic flux density or  $B_{\text{eff}}$  was computed with the magnetograph equation under the weak field approximation using the same method as Domínguez Cerdeña et al. (2003a). The magnetograms thus obtained are equivalent to the routine magnetograms (e.g., that obtained with the MDI

instrument on board of SOHO<sup>5</sup>), if we exclude the velocity fields. Figure 2 displays both magnetograms with the same scale of magnetic flux densities. At first sight, both images are similar with the exception that the signals found in visible are larger than the signals found in IR. Indeed, this is the first important difference. Since only the IN fields are of interest here, the network region pointed by a circle in the lower left part of our FOV was discarded from the analysis by rejecting pixels with flux densities larger than 20 G in the visible and 10 G in the IR. The noise levels turned out to be 2 G in the visible and 1 G in the IR. The method to estimate the noise is detailed in Domínguez Cerdeña et al. (2003b). The unsigned flux density obtained from pixels in the FOV with flux density below the upper limit and above noise was,

$$\overline{|B_{\text{eff}}|} = \begin{cases} 3.0 \text{ G, for Fe I } \lambda 6302.5 \text{ \AA,} \\ 1.5 \text{ G, for Fe I } \lambda 15648 \text{ \AA.} \end{cases} \quad (1)$$

In both cases the pixels with signals cover 45% of the total FOV (the rest of the pixels were set to zero in the calculation of  $\overline{|B_{\text{eff}}|}$ ). Under the same conditions of noise and spatial resolution, the measurements in the visible detect more flux than in the IR. This suggests that visible and IR lines trace different magnetic structures. The difference of flux is conspicuous, and one may be tempted to ascribe it to the approximations used for  $B_{\text{eff}}$ . However, more elaborated techniques show the same behavior (ME inversions in Sánchez Almeida et al. 2003a; Domínguez Cerdeña 2004, and §5).

Some magnetic flux concentrations are very similar in both magnetograms (squares in the upper part of Figure 2) but some others differ (see the other two squares). There are structures having one polarity in the IR magnetogram and the opposite in the visible one. This effect is evident even in the network area with large polarization signals (see the circle in Fig. 2). Such a result can be considered as an additional evidence of the different sensitivity to magnetic fields of the visible and the IR lines.

The magnetic fields in the visible magnetogram (Fig. 2 right) exhibit a preferred polarity while the IR magnetogram (Fig. 2 left) looks well balanced. The signed flux was measured to be,

$$\overline{B_{\text{eff}}} = \begin{cases} -2.0 \text{ G, for Fe I } \lambda 6302.5 \text{ \AA,} \\ -0.1 \text{ G, for Fe I } \lambda 15648 \text{ \AA.} \end{cases} \quad (2)$$

This imbalanced flux is similar to that measured in other visible observations (e.g., Lites 2002; Domínguez Cerdeña et al. 2003b). Yet, Khomenko et al. (2003) found almost no signed flux using the same IR lines (they observed 0.2 G).

All these results indicate that visible and IR lines may trace different magnetic structures, as conjectured by Sánchez Almeida & Lites (2000); Socas-Navarro & Sánchez Almeida (2003).

#### 4. DATA ANALYSIS

In order to infer the magnetic field strengths from the observations, we carried out an inversion of the Stokes profiles under the MISMA hypothesis. Micro-Structured Magnetized Atmospheres (MISMAs) were introduced for the first time by Sánchez Almeida et al. (1996), with the objective of reproducing the asymmetric Stokes profiles observed in most solar structures. Unresolved optically thin microstructures naturally render asymmetric Stokes profiles. The

MISMA scenario turns out to be an appropriate scheme of analysis since the observed quiet Sun Stokes profiles are very asymmetric, and it has been shown to work with the asymmetries of Fe I  $\lambda 6301.5 \text{ \AA}$  and Fe I  $\lambda 6302.5 \text{ \AA}$  (Sánchez Almeida & Lites 2000). In this section we give a description of the procedure followed to invert the data.

##### 4.1. PCA classification

We only analyze those Stokes  $V$  profiles clearly above noise. A threshold of three times the noise level was chosen in order to separate clear polarization signals from noisy profiles. Pixels with profiles whose peak polarization is above the threshold in both the IR and the visible data cover 40% of the FOV. This data set includes some 2280 pixels.

Following Sánchez Almeida & Lites (2000, § 3.2) the Stokes  $V$  profiles in the selected data set were classified using a principal component analysis algorithm (PCA). The aim is twofold. On the one hand, it reduces the number of representative profiles and, on the other hand, it provides low noise profiles to perform inversions used as initialization for the inversion of individual Stokes profiles. The classification is carried out simultaneously for the visible and the IR Stokes  $V$  profiles. The profiles of the four lines were scaled to the blue lobe of the Fe I  $\lambda 6302.5 \text{ \AA}$  Stokes  $V$  profile. The PCA method gives 38 classes. All profiles with large polarization signals were included in one single class to avoid contaminating the other classes with network profiles. The Stokes  $V$  threshold was chosen to be  $1\%I_c$  in the visible, and this special class includes all profiles from the network patch in the bottom left of our map (see Fig. 2). The large number of classes compared with those obtained for visible lines by Sánchez Almeida & Lites (2000, 10 classes) or for IR lines by Khomenko et al. (2003, 8 classes) is due to the combination of the different asymmetries found in the Stokes  $V$  profiles of the two pairs of lines. Note that, in general, the classes found in this work do not correspond to those obtained by Sánchez Almeida & Lites (2000) and by Khomenko et al. (2003).

We represent each class with the average of all profiles corresponding to the class. The individual profiles are not scaled to carry out the average. We only multiply them by the sign of the blue lobe of Fe I  $\lambda 6302.5 \text{ \AA}$ . Some of these classes are shown in Figures 3 and 4 (the dots). There is a clear improvement in the signal to noise ratio (S/N, defined as the maximum of the unsigned Stokes  $V$  profile divided by the noise) from the individual profiles to those representing the class. The individual profiles have a typical S/N between 3 and 10, whereas the two first classes have a S/N of 100. The IR profiles from classes 0 and 4 have tails extending far out from their extremes, as those predicted by Socas-Navarro & Sánchez Almeida (2003). These tails come from the contribution of kG field strengths. Such profiles are similar to class 0 in Khomenko et al. (2003, Fig. 1). The first 6 classes include 42% of the total number of profiles. One conspicuous fact is that some classes (e.g., classes 11 and 20) show one polarity in the visible and the opposite in the IR. Such a result was expected from the magnetograms in Figure 2. Approximately 20% of the profiles show the effect (see also Sánchez Almeida et al. 2003a).

##### 4.2. MISMA inversion

The MISMA inversion code is described by Sánchez Almeida (1997). We will follow a strategy similar

<sup>5</sup> See <http://sohowww.nascom.nasa.gov/>.

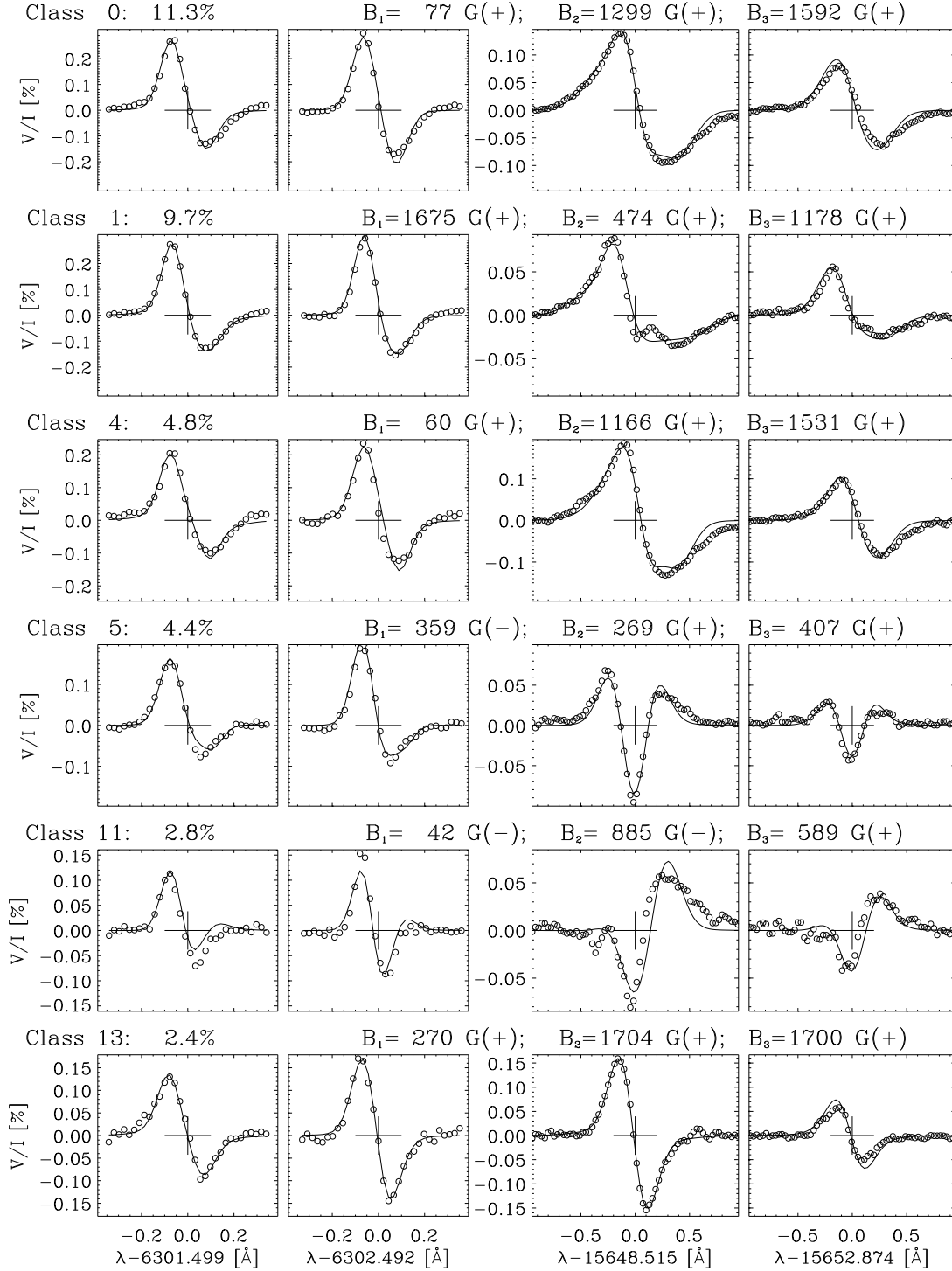


FIG. 3.— Some representative classes of observed Stokes  $V$  profiles showing the large variety of asymmetries produced by the quiet Sun magnetic fields. The circles represent the observed profiles and the solid lines the fits with MISMA model atmospheres. The header on top of each row displays the class number, the percentage of profiles belonging to the class, and the magnetic field of the three MISMA components at the base of the photosphere, sorted in order of decreasing mass. The polarity of the magnetic fields is indicated by plus and minus signs.

to Sánchez Almeida & Lites (2000). Here we summarize the main characteristics of the underlying model atmospheres:

1. There are four different components, one non-magnetic and three magnetic. Note that the inversion of visible lines performed by Sánchez Almeida & Lites (2000) require two magnetic components. As

Sánchez Almeida et al. (1996, §4.2) discuss, it is impossible to reproduce even the mildest observed asymmetries with only one component. Here we need one additional component to characterize the weak magnetic field strength revealed by the IR lines (Lin & Rimmele 1999; Khomenko et al. 2003;

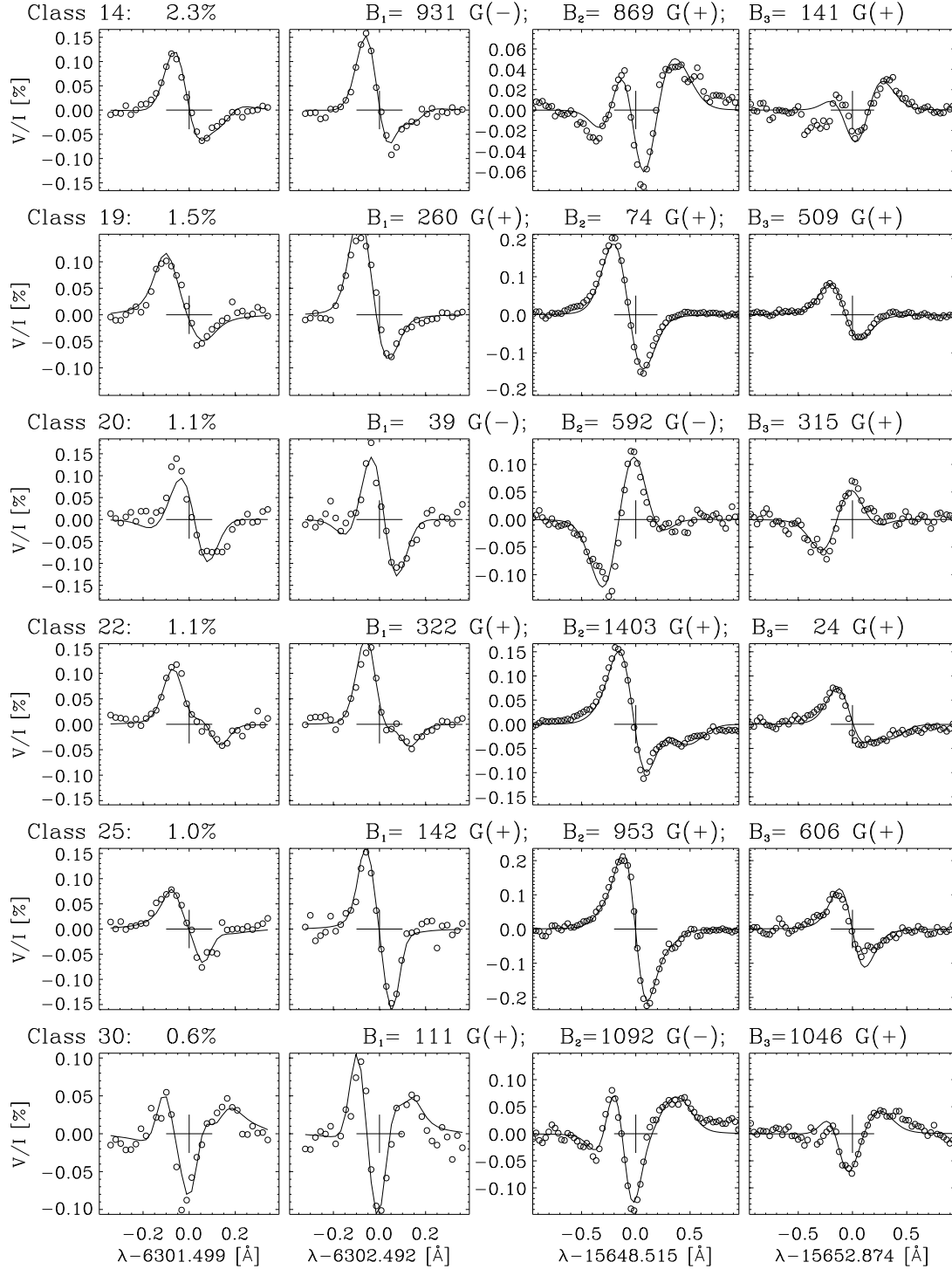


FIG. 4.— Same as Figure 3 for 6 additional classes.

Sánchez Almeida et al. 2003a). The components are embedded in a background producing unpolarized stray light.

2. The magnetic fields are vertical, along the line of sight. Since the observed Stokes  $Q$  and  $U$  signals are rarely above the noise level, it is reasonable to assume the inclination of the magnetic field to be

$0^\circ$  or  $180^\circ$ . The inversions were performed only for Stokes  $I$  and Stokes  $V$ . This approach allows us to compute longitudinal magnetic fields, however, the observations are compatible with inclined fields producing a linear polarization hidden by noise (see Sánchez Almeida & Lites 2000, § 4.7). The implications of this assumption are discussed in § 6.2.

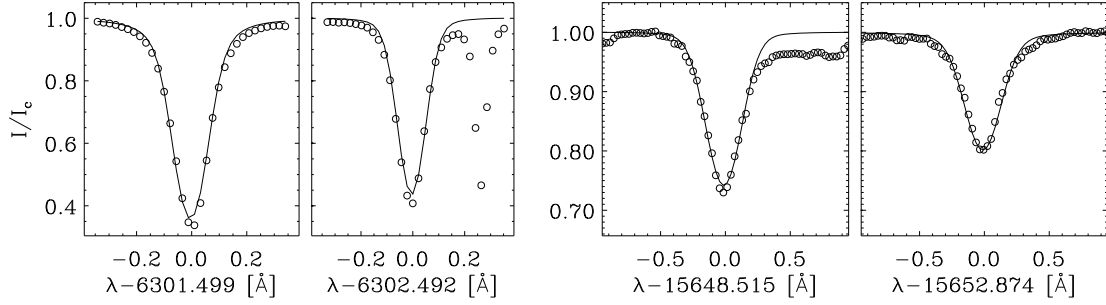


FIG. 5.— Example of a fit of the Stokes  $I$  profiles of the four lines. The circles represent the observed profiles, and the solid lines are the fits. Note the two strong telluric blends in the red wings of Fe I  $\lambda 6302.5$  Å and Fe I  $\lambda 15648$  Å.

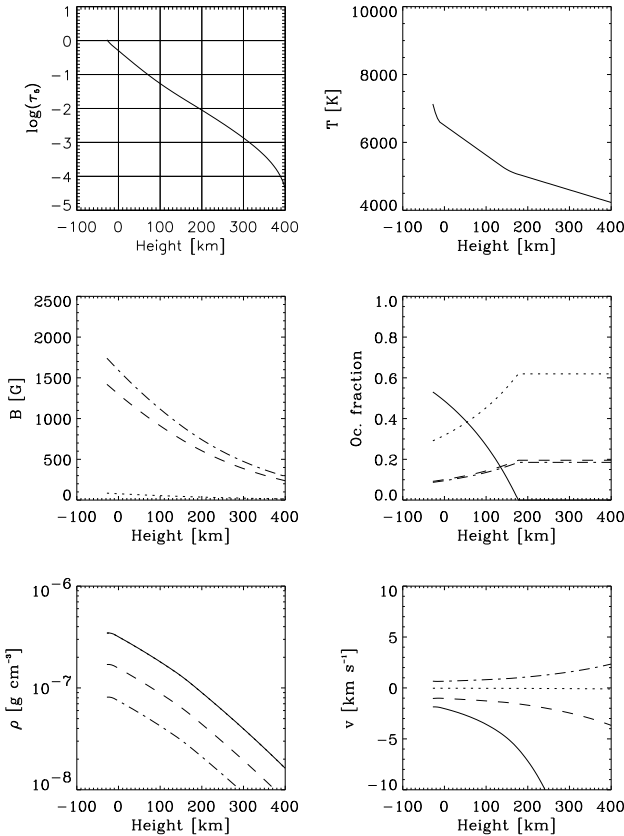


FIG. 6.— MISMA model from the inversion of class 0. The six panels show the variation with height of different physical parameters of interest. From left to right and top to bottom: the continuum optical depth at 5000 Å, the temperature, the magnetic field strength, the occupation fraction, the density, and the velocity along the field lines. The parameters are displayed for the four components except the optical depth: the solid line corresponds to the non-magnetic component, and the dotted, the dashed, and the dot-dashed lines to the three magnetic components. Note that the spectral lines are formed between 100 km and 300 km, so that the properties of the atmosphere outside this range are not constrained by the observations and therefore are not reliable.

3. The temperature of the components is forced to be the same. Since the magnetic structures are optically thin the radiative exchange between components is very efficient, washing out temperature differences in seconds.
4. The four components are in lateral pressure balance.

## 5. Motions are only allowed along magnetic field lines.

The temperatures are retrieved at four fixed heights in the atmosphere. The parameters characterizing each component are set at the bottom of the model atmosphere. They are the magnetic field strength, the occupation fraction, the bulk velocity, and the broadening parameter. The stratification of these parameters is obtained under the assumption of hydrostatic equilibrium and horizontal pressure balance. Three parameters account for the stray light, and another one parametrizes both the solar macroturbulence and the instrumental broadening due to limited spectral resolution. Despite the fact that the spectral resolution in the visible and the IR differ by 30 %, one can use a single macroturbulence for the two wavelength domains because the macroturbulence inferred from the inversions is completely dominated by true solar motions rather than instrumental smearing. The total number of free parameters amounts to 25. They are used to fit some 400 observables (each wavelength position of the Stokes  $I$  and  $V$  profiles of the four lines).

An example of the fit to the intensity profiles is shown in Figure 5. The observed profiles (circles) exhibit line blends. These are a telluric line close to the red wing of Fe I  $\lambda 6302.5$  Å, a solar Fe I line at 15647.3 Å, and an unidentified possibly telluric line in the red wing of Fe I  $\lambda 15648$  Å. To avoid the contamination by these blends, the Stokes  $I$  profiles at the wavelengths of the blends are excluded from the fit. There are also two OH bands of solar origin close to Fe I  $\lambda 15652$  Å, however, these bands are only visible in cool solar regions such as sunspots. The intensity profiles in Figure 5 are those from class 0.

All models have three magnetic components. In order to distinguish between them, we denote them as first, second and third components. The first component is that carrying the largest mass, as was defined by Sánchez Almeida & Lites (2000), and it is followed by the second and the third. If the three components would have the same magnetic field strength, the first would be the one producing the largest polarization signal.

Figure 6 displays the model MISMA of class 0 (see the Stokes  $V$  in Fig. 3). The different physical parameters of the non-magnetic, the first, the second, and the third magnetic components are plotted with solid, dotted, dashed and dot-dashed lines, respectively. The first magnetic component presents a weak magnetic field strength ( $\sim 100$  G at the base of the photosphere), while the other two have strong field strengths (larger than 1 kG). The density of the first magnetic component is the same as for the non-magnetic com-



ponent (Fig. 6 bottom-left panel) whereas the other two components have much lower density. The reduction is forced by the coupling between field strength and density produced by the lateral pressure equilibrium. The higher the magnetic field the lower the gas pressure and, for the same temperature, the lower the density.

## 5. RESULTS

Figures 3 and 4 show the fits produced by the MISMA inversion of 12 representative classes. All kinds of observed profiles are properly reproduced with three magnetic components per resolution element.

From now on, all results correspond to a single height in the atmosphere. We select the base of the quiet Sun photosphere, defined as the height where the total pressure equals to  $1.3 \times 10^5 \text{ dyn cm}^{-2}$ . Invoking lateral pressure balance among the individual model MISMA, this definition sets a single geometrical height for all the inversions, and it corresponds to the height where the continuum optical depth is one in the 1D quiet Sun model atmospheres (e.g., Maltby et al. 1986). The study is focused on two particularly important physical parameters, namely, the magnetic field strength and the occupation fraction. The latter corresponds to a volume filling factor.

The magnetic field strength inferred from the MISMA inversion of each class is also given in Figures 3 and 4. The magnetic field of the components are denoted as  $B_1$ ,  $B_2$  and  $B_3$ , in order of decreasing mass. Very often the inversions require one component with a sub-kG field strength and two with strong kG fields. Such a behavior is typical of the most abundant classes (e.g., classes 0, 1, 4). The Fe I  $\lambda 15648 \text{ \AA}$  Stokes V profiles of these classes are similar to that expected from the synthesis by Socas-Navarro & Sánchez Almeida (2003). The lobes of the profiles have a splitting equivalent to that produced by a weak field, however, they exhibit extended wings characteristic of strong fields. Some other classes have all components with fields in the range clearly below 1 kG (e.g., classes 5, 19, 20). In this case, there are no extended wings in the profiles of Fe I  $\lambda 15648 \text{ \AA}$ . Finally, note the presence of very asymmetric profiles. The IR profiles tend to have a higher degree of asymmetry. Some 28% of the analyzed pixels present IR profiles with three lobes (e.g., class 5). We found a fraction similar to that observed by Khomenko et al. (2003, 30%). There is also a small fraction of very asymmetric IR profiles with four lobes (3%, classes 14 and 30), while there are only a few visible profiles with three lobes (3%, e.g., class 30).

The model atmospheres obtained from the classes were used to initialize the inversion of the individual Stokes V profiles belonging to the class. From this moment on we refer only to results obtained from the inversion of the 2280 individual profiles.

### 5.1. Magnetic field strength and magnetic flux

The histograms of the distribution of magnetic field strength obtained from the inversion of the individual profiles are displayed in Figure 7. They show the percentage of pixels within bins of 50 G for the different components. The solid, the dashed, and the dotted lines distinguish the first, the second, and the third magnetic components, respectively. The results from the network patch were omitted (see § 3). The first component tends to have much weaker fields than the other two and it has a shape similar to the distribution obtained by Khomenko et al. (2003) using only

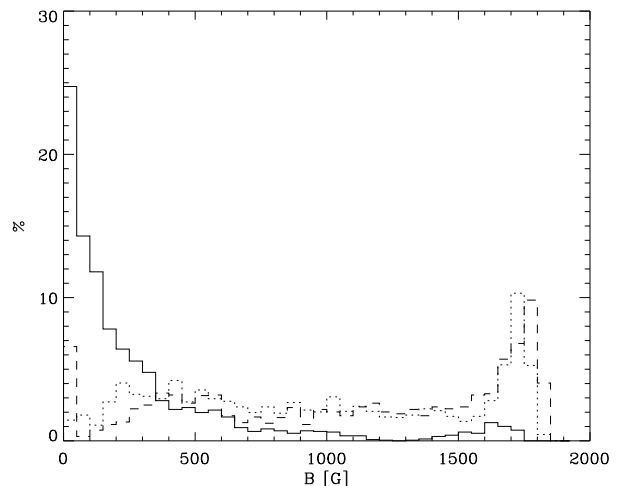


FIG. 7.— Histograms of the magnetic field strength at the base of the photosphere, determined from inversion of the individual Stokes  $I$  and  $V$  profiles. The first, the second and the third components are plotted with solid, dotted and dashed lines, respectively.

IR lines. The mean field obtained for this component is 290 G. The second and the third components show the same behavior as the histograms obtained with visible lines by Sánchez Almeida & Lites (2000). They have mean fields of 970 and 1100 G respectively. Despite the similarity between the magnetic field strengths of the second and the third components, they are well separated by the inversion code. There are large differences of Doppler shift between them; 85 % of the models are separated by more than  $500 \text{ m s}^{-1}$  at the base of the photosphere, and this difference increases substantially in the heights of formation of the spectral lines. (See also § 6.3.)

The top panels of Figure 8 show the maps of field strength for the three magnetic components. The magnetic field of the first, the second and the third components are displayed from left to right. The network point (bottom left) is almost the only feature with strong kG fields in the first component. Most of the pixels show at least one component with strong fields. More specifically, 92% of the analyzed pixels possess at least one field larger than 500 G while the fraction with field strengths above 1 kG is 74%.

The map with the filling factor of the magnetic fields (the sum of occupation fractions of the three components) is displayed in the bottom left panel of Figure 8. It goes from 10% in network points to 0.5%, and the mean value is approximately 4%. If we consider the whole FOV (all values in the pixels not analyzed are set to zero), and we exclude the network profiles, the measured magnetic fields fill only 1.5% of the IN region.

The bottom right panel of Figure 8 gives the map of the total magnetic flux density computed as the product of the occupation fraction times the magnetic field strength. Note that the flux density is given in G (or  $\text{Mx cm}^{-2}$ ), thus it can be directly compared with other measurements with different pixel size or FOV. Most parts of the analyzed surface present a flux density larger than 25 G (sum of the three components). Considering the whole map, we measure a total flux density of 9.6 G which is similar to the value obtained by Socas-Navarro & Sánchez Almeida (2002) or Lites (2002) with better spatial resolution.

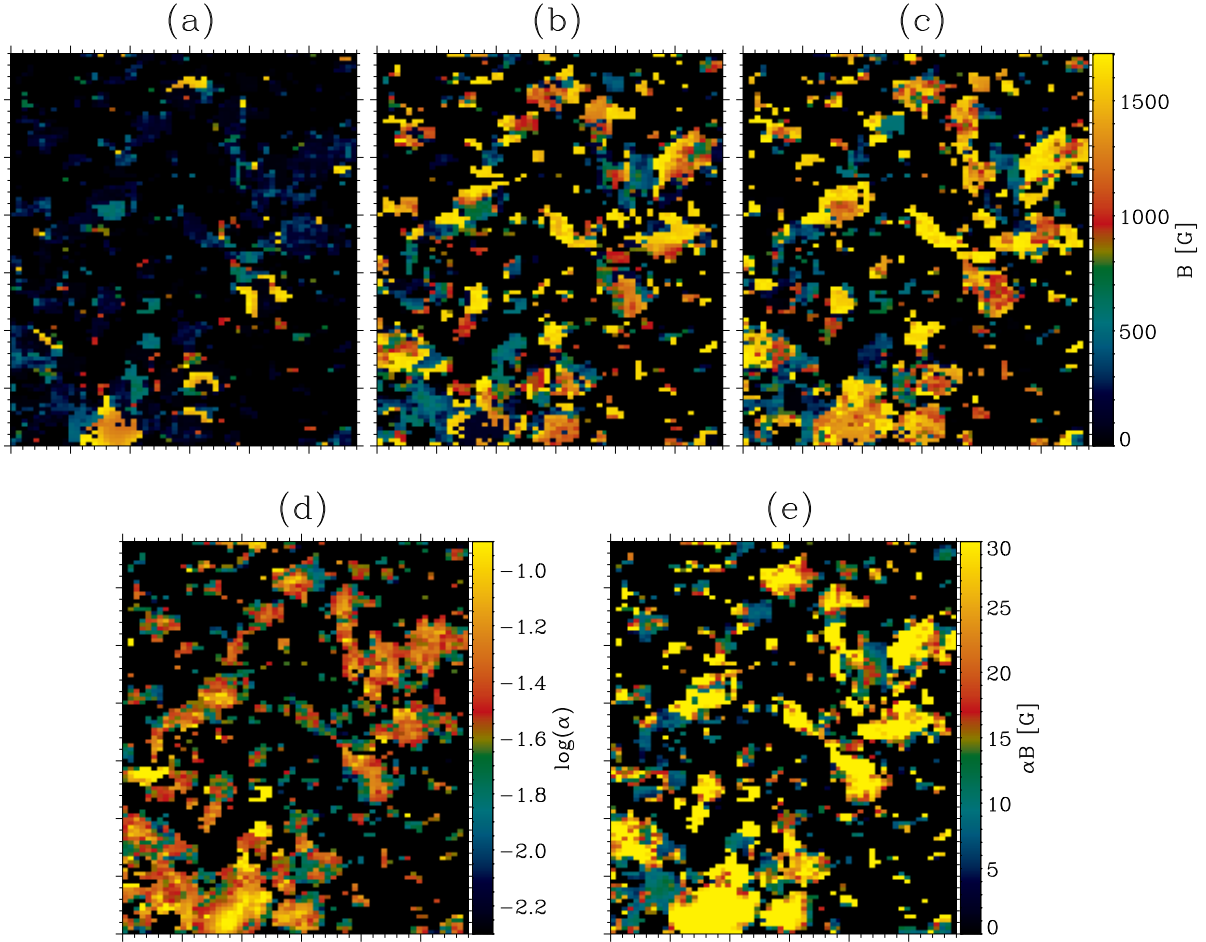


FIG. 8.— The three upper panels (a,b,c) show maps of the magnetic field strength at the base of the photosphere of the first, the second and the third components, respectively. The bottom left panel (d) gives the occupation fraction (filling factor) of the three components all together in a logarithmic scale. The total unsigned magnetic flux is shown in the bottom right panel (e). It is saturated at 30 G. Black regions correspond to pixels with polarization signals too low to be inverted. The separation between minor tickmarks is one arcsec.

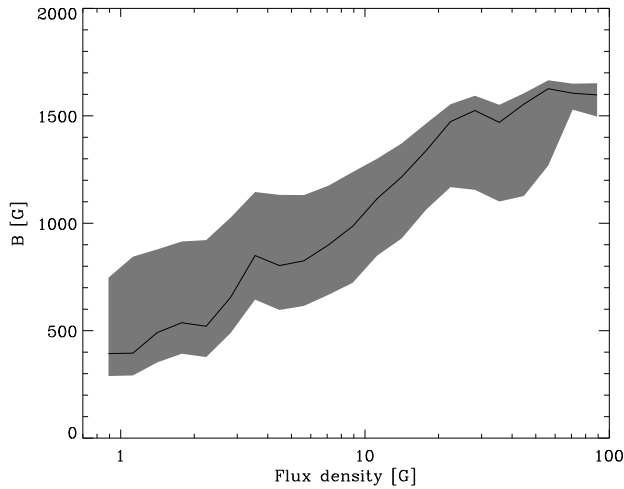


FIG. 9.— Mean magnetic field strength of all components as a function of the magnetic flux density. The shaded area gives the standard deviation above and below the mean value.

Figure 9 shows the variation of the magnetic field strength of all components with the magnetic flux density. The shaded area represents the standard deviation above and below the mean value. A difference between the two standard deviations reveals the asymmetry between the distribution of field strength above and below the mean value. There is a strong tendency for the field strengths to weaken when the magnetic flux decreases. Sánchez Almeida & Lites (2000) obtained a less pronounced dependence, but their lowest detectable flux density was 10 G while in this work it decreases down to 1 G.

### 5.2. Mixed polarities

50% of the analyzed pixels can be fitted only with mixed polarities in the model MISMA. Since we fit 40% of the total pixels, this fraction corresponds to 20% of the FOV. This large amount of pixels includes all profiles with three or four lobes in the IR and/or visible (30%), and also those profiles with a clear polarity in the visible Stokes profiles and the opposite in the IR profiles (20%). We find that the fields of those pixels are weaker than the rest. Figure 10 shows the histograms of the field strength as in Figure 7 but only for models including mixed polarities. All components show fields weaker than in Figure 7. From the first, the second and the third magnetic

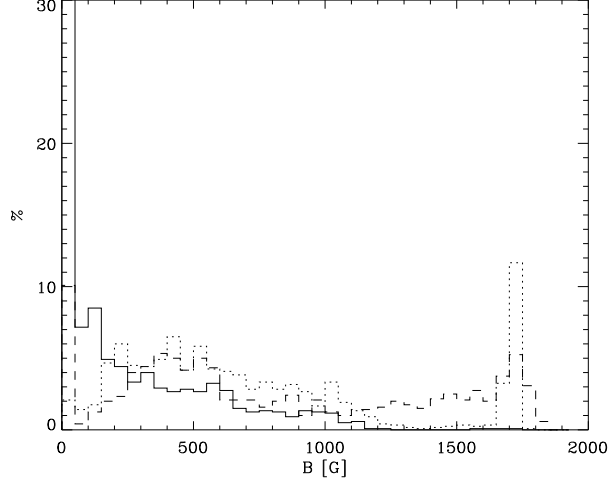


FIG. 10.— Same as Figure 7 but only for those pixels with mixed polarities in the resolution element.

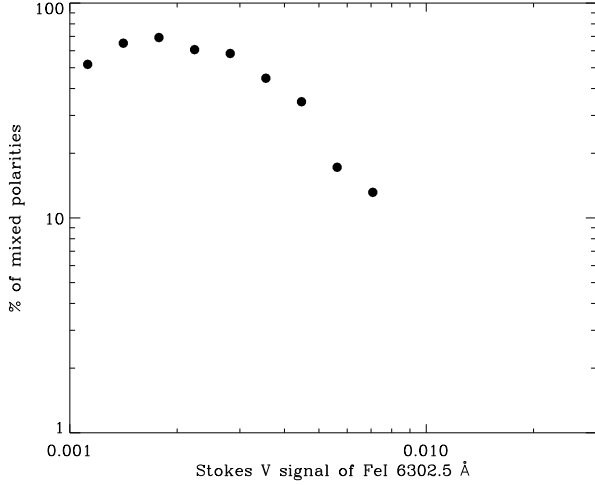


FIG. 11.— Percentage of pixels with mixed polarities versus the Stokes  $V$  signal of Fe I  $\lambda 6302.5$  Å.

components we retrieve a mean field of 250, 700 and 880 G, respectively.

Figure 11 gives the percentage of mixed polarities as a function of the Stokes  $V$  signal of Fe I  $\lambda 6302.5$  Å. The weaker the polarization signal the larger the fraction of mixed polarities. This behavior was already noted by Sánchez Almeida & Lites (2000) and Socas-Navarro & Sánchez Almeida (2002) but they obtained a maximum fraction of 25%. The fraction in Figure 11 flattens to 65% for Stokes  $V$  lower than 0.002.

### 5.3. Distribution of field strengths

We compute the probability density function (PDF) of the magnetic field strength from the magnetic field and occupation fractions procured by the MISMA inversions of the individual profiles. The PDF gives the probability of finding a specific magnetic field strength in the observed IN region. The range of magnetic fields from 0 to 2000 G was divided into bins of 50 G. Each individual intrinsic field  $B$  is assigned to one bin. The probability to find the magnetic field of a

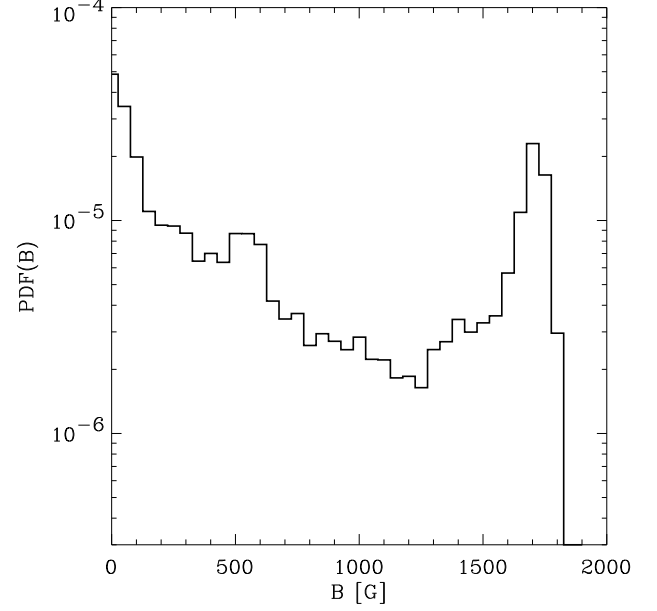


FIG. 12.— Probability density function of the magnetic field strength at the base of the photosphere as inferred from Zeeman signals.

single bin is the sum of the occupation fractions of all pixels with  $B$  belonging to this bin. We normalize the PDF so that its integral provides the filling factor of magnetic structures in the IN region assuming that the pixels without signals have no magnetic field strength.

The PDF of the magnetic field strength condenses information on the quiet Sun magnetism that can be used for comparisons with other observations and numerical simulations. The first moment  $\langle B \rangle$  is connected with the magnetic flux density and the second moment provides the magnetic energy density  $\langle B^2 \rangle / 8\pi$ :

$$\langle B \rangle = \int_0^\infty B \text{PDF}(B) dB, \quad (3)$$

$$\langle B^2 \rangle = \int_0^\infty B^2 \text{PDF}(B) dB. \quad (4)$$

Figure 12 shows the PDF of our IN region. Once again, we have avoided those pixels belonging to the small network patch in the FOV. The shape of the PDF is to be expected from the histogram of Figure 7. Most of the filling factor is concentrated in the weak fields, while most of the magnetic flux comes from the strong fields. Table 3 summarizes the properties of the PDF. It shows the filling factor, the flux density, the fraction of flux, and the fraction of energy in four different ranges of magnetic field strengths, i.e., the full range, the weak fields ( $B < 500$  G), the strong fields ( $B > 500$  G), and the kG fields ( $B > 1000$  G). Three quarters of the total observed flux and 90% of the magnetic energy is in the kG fields, despite they represent only 30% of the total filling factor.

There is an accumulation of field strength between 1600 and 1800 G. It may be due to the combined effect of a magnetic intensification mechanism plus the existence of an upper limit that the magnetic field strength cannot exceed. This limit of 1800 G corresponds to a magnetic pressure equal to the gas pressure of the non-magnetic plasma at the base of the photo-

TABLE 3  
FILLING FACTOR, MAGNETIC FLUX DENSITY AND MAGNETIC ENERGY DENSITY OF THE PDF  
IN FIGURE 12.

Range	filling factor [%]	flux density [G]	energy density [erg cm <sup>-3</sup> ]	fraction of flux [%]	fraction of energy [%]
total	1.50	9.6	500	100	100
B<500 G	0.87	1.2	10	10	2
B>500 G	0.63	8.4	490	90	98
B>1000 G	0.42	7.0	450	75	90

sphere. The magnetic intensification mechanism would try to pile up magnetic fields right before the upper limit.

#### 5.4. Signed flux

When we average over the FOV, the *signed* magnetic flux does not cancel completely. The flux density, taking into account the direction of the magnetic field, turns out to be  $-3.5$  G. This net flux was expected from the results in § 3 (equation [2]). Lites (2002) already observed the presence of an imbalanced flux in almost all the observation he studied. He measured an imbalance (defined as the signed flux divided by the unsigned flux) between  $-0.20$  and  $+0.48$ , and found a direct correlation between the imbalance of the IN fields and the imbalance of the network fields around them. Our imbalance is  $-0.36$  and our network region is negative almost everywhere. Figure 13 shows the PDF of the signed magnetic field strength, i.e., the magnetic field strength times the sign of the vertical component of the magnetic field. There is a large contribution of strong fields in the negative flux part of the PDF, while the positive part has a continuous fall off from weak to strong fields. The weak fields are well balanced while the strong fields have a preference toward negative polarity, i.e., the same polarity as the network patch. For fields weaker than 500 G the imbalance is only  $-0.09$ , and for field strengths

stronger than 1 kG the imbalance is  $-0.5$ . Socas-Navarro et al. (2004) already observed the preference of the strong fields towards one polarity, and Figure 13 shows a clear observational evidence of such an effect.

#### 6. CRITICAL ASSESSMENT OF SOME ASSUMPTIONS AND RESULTS

Some of the properties of the observational material used in the work, and the assumptions of the inversion, are not ideal but dictated by feasibility. In order to strengthen the validity of the results, we devote this section to analyze the assumptions and results that may be more critical.

##### 6.1. Time lag between IR and visible data sets

Our visible and IR spectra average the IN properties in spatial scales of  $1''.5$  arcsec and temporal scales of 30 sec (§ 2). The time lag between visible and IR spectra would be of concern only if this spatio-temporal average changes significantly during 1 min. Fortunately, large changes of the average properties are not expected for a number of reasons. First, the integration time of the individual measurements smears out the short time-scale variations of the IN fields, and only variations in the range between 30 sec and 1 min are of concern. Second, low spatial resolution observations of IN magnetic fields show how many structures remain stable for tens of minutes, and longer (e.g., Zhang et al. 1998; Domínguez Cerdeña et al. 2003b). Obviously, our time lag does not represent a problem for these structures. In view of the results coming from high resolution observations and numerical simulations of magneto-convection, this time stability cannot not be interpreted as the stability of individual magnetic structures but the stability of the average properties. For example, a strong granular downdraft lives longer than the granules and, during its lifetime, it continuously advects magnetized plasma towards a specific point of the solar surface (Rast 2003). Observed with low resolution, one would detect a magnetic patch that remains in place for a long period of time, despite the fact that it is formed by many small-scale short-lived magnetic structures that are continuously advected and engulfed by the downdraft. Finally, for the average magnetic properties to present significant variations during the time lag, the typical velocities of the magnetized plasma would have to be unphysically high. Consider the horizontal velocities required to sweep out during the time lag all magnetic elements existing in a resolution element. In this case the magnetic structures in the same resolution element of the visible and IR maps will be completely different, questioning any interpretation based on their simultaneity. The required velocities would have to be of the order of the speed needed to cross a resolution element during the time lag, i.e.,  $18 \text{ km s}^{-1}$ . Such speed is too high to be common. It is supersonic, and much larger than the observed vertical velocities. Obviously, the lack of simultaneity

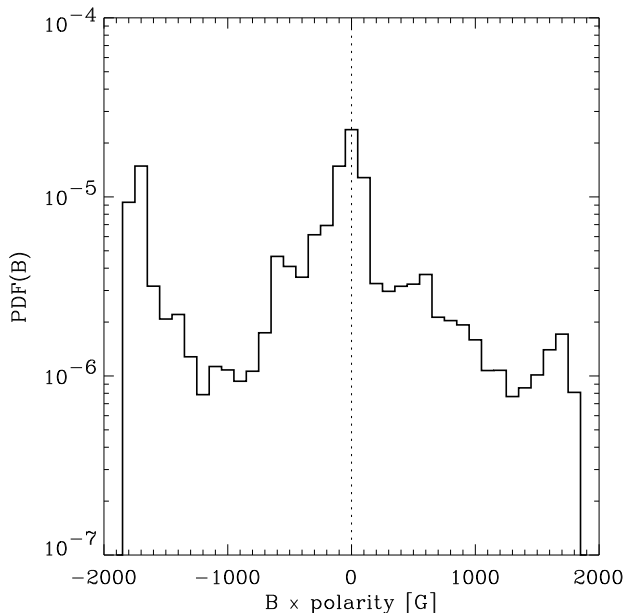


FIG. 13.— PDF of the magnetic field strength times the sign of the polarity of the flux. The vertical dotted line points out  $B = 0$  G.

becomes more problematic as the spatio-temporal resolution of the observation improves.

From our point of view, the spatial and temporal integration of the measurements represents a problem more serious than the time lag and the small spatial resolution differences that may remain between the IR and the visible data sets. The polarization detected in each resolution element results from adding up contributions from many magnetic structures having very different properties. Our inversions provide only a crude representation of what may be happening in the real Sun. This problem, however, is not specific of our work but affects all previous observational works on the IN magnetic fields. In the case of the MISMA inversions the problem is ameliorated because a sketchy model MISMA actually represents many different underlying atmospheres, including very complex ones. All those atmospheres having the same average properties produce the same spectrum, and these average properties are the ones that the inversions retrieve (see the discussion in Sánchez Almeida & Lites 2000, § 5).

### 6.2. The inclination of the magnetic fields

The inversions were carried out under the assumption of longitudinal magnetic fields, which minimizes the number of free parameters and simplifies the inversions. This assumption, however, biases the inferred  $\text{PDF}(B)$ . Fortunately, the importance of the bias can be estimated and it turns out to be small. If a magnetic field has an inclination  $\gamma$  with respect to our vertical line-of-sight, the Stokes  $V$  spectrum remains approximately as in the case of vertical field but scaled with the factor  $\cos \gamma$ . This is a general property of the radiative transfer equation, and is not restricted to weak fields on plane-parallel atmospheres (see Sánchez Almeida & Trujillo Bueno 1999, § 3.1). Consequently, if an observed Stokes  $V$  profile is reproduced with the wrong inclination, all the parameters of the inversion would remain the same except for the occupation fraction  $\alpha(B)$ . The occupation fraction provides a global scaling factor for the Stokes  $V$  profiles, and so it absorbs the full bias. Our  $\text{PDF}(B)$  is biased because it is based on occupation fractions underestimated by a factor  $|\cos \gamma(B)|$ ,

$$\text{PDF}(B) = N^{-1} \sum_{i=1}^{n(B)} |\cos \gamma_i(B)| \alpha_i(B), \quad (5)$$

with the subscript  $i$  denoting one of the  $n(B)$  pixels with a field strength  $B$ , and the symbol  $N$  standing for a normalization constant. Obviously,  $\text{PDF}(B)$  sets a lower limit to the true  $\text{PDF}^*(B)$ ,

$$\text{PDF}^*(B) = N^{-1} \sum_{i=1}^{n(B)} \alpha_i(B) \geq \text{PDF}(B), \quad (6)$$

since  $|\cos \gamma_i(B)| \leq 1$ . On the other hand, it is possible to set an upper limit by estimating the maximum inclination allowed by the noise in Stokes  $Q$  and  $U$ . Following, Sánchez Almeida & Lites (2000, § 4.7), we synthesize the linear polarization produced by our model atmospheres when the magnetic field of the three components is inclined. For each model MISMA we determine the largest inclination  $\gamma_u$  producing undetectable linear polarization, i.e., below the observational noise. If we use this inclination to correct the occupation fractions, one can define a new  $\text{PDF}_u(B)$  which represents an upper limit to the true  $\text{PDF}^*(B)$ ,

$$\text{PDF}_u(B) = N^{-1} \sum_{i=1}^{n(B)} \frac{|\cos \gamma_i(B)|}{|\cos \gamma_{ui}(B)|} \alpha_i(B) \geq \text{PDF}^*(B), \quad (7)$$

where the inequality follows from the fact that  $|\cos \gamma_i|/|\cos \gamma_{ui}| \geq 1$  for all  $i$ . We find that the unsigned flux corresponding to  $\text{PDF}_u(B)$  is only 25% larger than the flux of  $\text{PDF}(B)$ , indicating that the assumption of vertical fields have a very limited effect on the PDF estimated in the paper.

### 6.3. Need for three magnetic components

Due to the similarity between the magnetic field strengths of the second and the third magnetic components, one may wonder whether they are really needed to reproduce the line shapes. Moreover, if they are not needed, the existence of mixed polarities may be an artifact since the signals of the two components cancel out producing no observable residual. As we stress in § 4.2, the three components are needed. Here we elaborate on the reasons. Reproducing the Stokes  $V$  asymmetries of the visible lines requires two magnetic components, even for the mildest asymmetries characteristic of the network. One single magnetic component produces Stokes  $V$  area and the peak asymmetries of the same magnitude, in contradiction with the observations (Sánchez Almeida et al. 1996, p. 545). Somehow unexpectedly, Sánchez Almeida & Lites (2000) find that these two components are enough to explain not only the mildest asymmetries, but the whole range of observations including extreme profiles with an even number of lobes. These two components have similar kG magnetic field strengths, but very different velocities (Sánchez Almeida & Lites 2000, Figs. 12 and 14). The large difference of velocities is demanded by the observed Stokes  $V$  asymmetries, and it is the reason why the inversion code is able to separate them. Here we analyze profiles similar to those reproduced by Sánchez Almeida & Lites (2000) and, consequently, a minimum of two magnetic components is needed. In addition, we also want to reproduce the IR lines which, according to the literature, indicate the existence of weak fields in the quiet Sun. A third weak magnetic field component was needed too. This argument does not imply that all the observed profiles necessarily require three components. It implies that the typical cases need three components (regular Fe I  $\lambda 6301.5$  Å and Fe I  $\lambda 6302.5$  Å, with Fe I  $\lambda 15648$  Å and Fe I  $\lambda 15652$  Å showing weak fields). It also implies that that typical Stokes  $V$  profiles have enough information to constrain the three components. Finally, it implies that if a single MISMA scenario is going to be used to reproduce all the asymmetries, it must contain three components.

### 6.4. The inferred magnetic field strengths

One of the main conclusions of this work is the co-existence of kG and sub-kG fields in resolution elements of  $1''.5$  as inferred from the simultaneous inversion of IR and visible Stokes profiles.

The use of visible lines to measure kG magnetic field strength has been criticized. The analysis of extremely noisy Stokes  $V$  profiles of Fe I  $\lambda 6301.5$  Å and Fe I  $\lambda 6302.5$  Å may induce a bias towards kG (see Bellot Rubio & Collados 2003), and the Stokes  $V$  profiles from the visible lines are the major tracers of the kG magnetic fields in our inversion. However, the kG that we infer are not produced by such a bias for a number of reasons. The classes have much less noise than the individual profiles, and yet the inversion yields as much kG of the individual profiles. The classes that yield at least one kG magnetic component represent 75% of the total pixels. They include the two main classes with a S/N

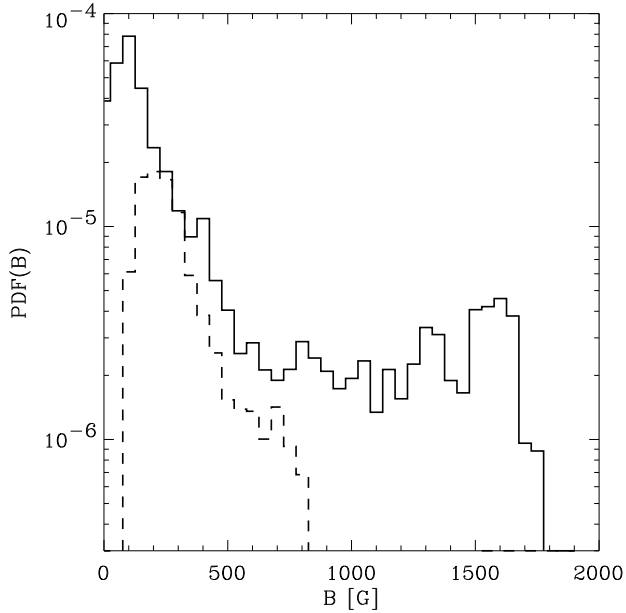


FIG. 14.— PDF of the magnetic field strength computed from the inversion of the IR profiles alone. The solid line is the PDF inferred from the inversion under the MISMA hypothesis, and the dashed line the PDF from the Milne-Eddington inversion.

larger than 100. Another 10 classes have S/N larger than 30, which ensures inversions without the bias pointed out by Bellot Rubio & Collados (2003).

Another way to test the consistency of our results is to invert only the IR lines to see whether it is possible to infer kG fields in the quiet Sun without visible lines. This inversion was performed in the same way as in § 4.2 but only for Fe I  $\lambda 15648$  Å and Fe I  $\lambda 15652$  Å with MISMA models including only 2 magnetic components (see more details in Domínguez Cerdeña 2004). The result of such analysis was a major magnetic component similar to the first component in Figure 7 and a second with weak and strong fields. A field stronger than 1 kG was found in 50% of the inverted pixels (those with the strongest IR signals). The strong fields were retrieved from the extended wing of the Stokes *V* profiles. Figure 14 gives the PDF obtained from these inversions. The strong field contribution is not as large as in Figure 12, but it still carries most of the magnetic energy and flux. The presence of fewer strong fields as compared to the full inversions including visible lines is due to the incompleteness of the information given by the IR lines, since most of the contributions from strong fields remains hidden by noise. The signed flux has a behavior similar to that of the full inversion described in § 5.4. It is more important for the fields stronger than 1 kG while the weak fields are balanced. Figure 14 also shows the PDF obtained from the Milne-Eddington inversion of the IR lines (the dashed line; see Sánchez Almeida et al. 2003a). This inversion was performed with a single magnetic component and shows only the weak field component.

## 7. DISCUSSION AND CONCLUSIONS

A new observational technique was used to study the quiet Sun magnetism. Simultaneous visible (Fe I  $\lambda 6301.5$  Å and Fe I  $\lambda 6302.5$  Å) and infrared (Fe I  $\lambda 15648$  Å and Fe I  $\lambda 15652$  Å) polarimetric observations were analyzed un-

der the assumption of Micro-Structured Magnetized Atmosphere (MISMA). We generate model MISMA models able to reproduce all kinds of asymmetries presented in the observed Stokes *V* profiles, even when there are clear differences in the asymmetries of the visible and the IR Stokes profiles. The model atmospheres have three magnetic components.

The simultaneous inversion of the visible and IR pairs reveals the co-existence of kG and sub-kG fields in the low photosphere. We have observed this combination of weak and strong fields in 74% of the pixels under study, which means 30% of the pixels of the FOV (see § 5.1). This was already observed by Sánchez Almeida et al. (2003a) from the separate inversion of the IR and visible lines, however, this work presents the first evidence of the co-existence of kG and sub-kG fields from a simultaneous inversion of lines in the two spectral ranges. From the three magnetic components, the one having most of the mass includes most of the weak fields. The two other components tend to show strong kG fields. The preference of the first component to have the weakest fields is due to the coupling between field strength and plasma density. The weaker the field the larger the density so that the component of weakest field tends to have the largest mass. The histogram of field strengths of these minor components (Fig. 7) looks similar to that obtained by Sánchez Almeida & Lites (2000), while the first component has a distribution similar to that obtained with the analysis of IR lines by Khomenko et al. (2003). This supports the hypothesis of Sánchez Almeida & Lites (2000) and Socas-Navarro & Sánchez Almeida (2002, 2003): the study of the quiet Sun magnetism with only visible lines or only IR lines biases the resulting field strengths; the IN fields must be studied combining Stokes profiles from both spectral ranges.

The inferred magnetic fields occupy 1.5 % of the total FOV. Other observations with better spatial resolution (1''; Socas-Navarro & Sánchez Almeida 2002; Khomenko et al. 2003) yield a total filling factor of 1 %. We obtain a larger value thanks to the combined use of the information from visible and IR lines, while all previous works used lines from a single spectral range. The filling factor inferred for the same observations used in this paper by Sánchez Almeida et al. (2003a) was only 0.85%. The difference is due to the different model atmospheres used to reproduce the observations. While here we use a realistic multicomponent model, Sánchez Almeida et al. (2003a) carried out Milne-Eddington inversions with a single magnetic component. Thus, the filling factors in pixels with mixed polarities (see § 5.2) are underestimated.

We have measured an average flux density over the FOV of 9.6 G (those pixels without polarization signals contribute to this average with zero field strength; § 5.1). This flux is similar to that obtained by analysis of visible lines with 1'' spatial resolution (see Socas-Navarro & Sánchez Almeida 2002; Lites 2002) while it is two times larger than the magnetic flux derived from IR lines (Khomenko et al. 2003). Albeit our observations have lower resolution (1.''5), the use of visible and IR lines reveals more magnetic structures than the use of lines from a single spectral range. The flux density is also larger than the magnetic flux obtained in § 3 using the magnetograph equation applied to a single line. A combination of factors explain such bias. First, we obtained magnetic field strengths larger than the saturation limit of the lines, thus the circular polarization signals are no longer proportional to the magnetic flux and equation (1) is a lower limit of the real flux. Second, the presence of mixed polarities (see § 5.2) produces

cancellation of polarization signals and the magnetic flux is underestimated. Third, the lines weaken in strong magnetic concentrations, leading to a well known diminishing of polarization signals (e.g., Harvey & Livingston 1969). Finally, the visible and IR signals often trace different concentrations co-existing in the resolution element. Then, combined inversions allow us to detect more flux than the inversion of one of the spectral ranges.

The inversion indicates the presence of mixed polarities in at least 20% of the FOV (§ 5.2). This is the largest fraction of mixed polarities obtained from direct measurements. The fraction of pixels with mixed magnetic polarities grows as the polarization signals weaken (Fig. 11). More than half of the profiles with Stokes  $V$  signal lower than 0.2% of the continuum intensity have mixed polarities.

We have estimated the probability of finding a given magnetic field strength in the quiet Sun, i.e., the probability density function of the magnetic field strength (PDF; § 5.3). It is largest for the weakest fields, however, an extended kG tail goes up to a limit around 1800 G. Despite the fact that the kG fields have only 30% of the total filling factor, they carry 75% of the total flux and 90% of the total magnetic energy.

There is a clear imbalance of the magnetic flux towards one polarity. We measure a signed flux density of  $-3.5$  G which is mostly due to the strong kG fields (§ 5.4). The signed PDF (Fig. 13) shows how the weak fields are well balanced whereas the strong fields have a clear preference for the negative polarity. This imbalanced flux has the same sign as the surrounding network, as it was already observed by Lites (2002). This imbalance is qualitatively similar to those imposed in some MHD simulations of granular convection (see Vögler 2003; Vögler & Schüssler 2003). These simulations have an initial unipolar field. The convection reprocesses this field to yield a continuous PDF with a clear imbalance in the strongest fields.

The MISMA inversion of the IR profiles alone also gives rise to a PDF with extended kG tail (§ 6.4). Such tail does not appear in Milne-Eddington inversions of the same profiles, which tend to select the component of weakest field in the resolution element.

The magnetic fields studied in this paper fill only 1.5% of the total FOV. The unsigned flux density that we mea-

sure is only a lower limit of the real flux. Larger fluxes are obtained in observations with better spatial resolution (Domínguez Cerdeña et al. 2003a,b; Sánchez Almeida 2003b) and, furthermore, measurements based on the Hanle effect are compatible with a flux density of 60 G or more (Sánchez Almeida et al. 2003b; Trujillo Bueno et al. 2004; Bommier et al. 2005). A large fraction of the magnetic structures remains undetected in Zeeman based observations. Based on our biased observations, we have produced a PDF with the distribution of magnetic field strengths. Obviously, this is not the real solar PDF. A natural step forward would be working out an unbiased PDF with the help of different measurements based on the Zeeman effect, the Hanle effect, and also MHD simulations. This work of synthesis is carried out in a separate paper (Domínguez Cerdeña et al. 2006). Despite these and other efforts, we are still far from having a complete picture of the quiet Sun magnetism. There is a reduced number of observations and each one is gathered with different instruments under different conditions. Thus, we need a survey of polarimetric data across many IN regions of the Sun, if we want to study the quiet Sun with a systematic and global point of view. Such data would allow us to start exploring the connection of the IN with active regions, the chromosphere and corona and, eventually, to follow the evolution of the IN with the solar cycle. Observations with better spatial and temporal resolution are mandatory. They are coming up thanks to the advent of new generation ground based and space-borne solar telescope (Keil & Avakyan 2003). These improvements, together with the development of more realistic numerical simulations, guarantee a rapid evolution of the field.

Thanks are due to the support astronomers and operators of THEMIS and VTT for help during the observation. The VTT is operated by the Kiepenheuer-Institut für Sonnenphysik, Freiburg, and the French-Italian telescope THEMIS is operated by CNRS-CNR, both at the Spanish Observatorio del Teide of the Instituto de Astrofísica de Canarias. The work has been partly funded by the Spanish Ministry of Science and Technology, project AYA2004-05792 and by the Deutsche Forschungsgemeinschaft through grant 418 SPA-112/14/01.

## REFERENCES

- Asplund, M., Nordlund, Å., Trampedach, R., Allende Prieto, C., & Stein, R. F. 2000, *A&A*, 359
- Ballesteros, E., Collados, M., Bonet, J. A., Lorenzo, F., Viera, T., Reyes, M., & Rodríguez Hidalgo, I. 1996, *A&AS*, 115, 353
- Bellot Rubio, L. R., & Collados, M. 2003, *A&A*, 406, 357
- Bommier, V., Derouich, M., Landi Degl'Innocenti, E., Molodij, G., & Sahal-Bréchet, S. 2005, *A&A*, 432, 295
- Bommier, V., & Rayrole, J. 2002, *A&A*, 381, 227
- Borrero, J. M., & Bellot Rubio, L. R. 2002, *A&A*, 385, 1056
- Borrero, J. M., Bellot Rubio, L. R., Barklem, P. S., & del Toro Iniesta, J. C. 2003, *A&A*, 404, 749
- Cameron, R., & Galloway, D. 2005, *MNRAS*, 358, 1025
- Cattaneo, F. 1999, *ApJ*, 515, L39
- Collados, M. 1999, in *ASP Conf. Ser. 184: Third Advances in Solar Physics Euroconference: Magnetic Fields and Oscillations*, 3–22
- Collados, M. 2003, *Proc. SPIE*, 4843, 55
- de Wijn, A. G., Rutten, R. J., Haverkamp, E. M. W. P., & Sütterlin, P. 2005, *A&A*, 441, 1183
- Domínguez Cerdeña, I. 2004, PhD thesis, Göttingen University, Göttingen
- Domínguez Cerdeña, I., Kneer, F., & Sánchez Almeida, J. 2003a, *ApJ*, 582, L55
- Domínguez Cerdeña, I., Sánchez Almeida, J., & Kneer, F. 2003b, *A&A*, 407, 741
- . 2006, *ApJ*, 636, 496
- Emonet, T., & Cattaneo, F. 2001, *ApJ*, 560, L197
- Grossmann-Doerth, U., Keller, C. U., & Schüssler, M. 1996, *A&A*, 315, 610
- Gurtovenko, E. A., & Kostik, R. I. 1981, *A&AS*, 46, 239
- Harvey, J., & Livingston, W. 1969, *Sol. Phys.*, 10, 283
- Harvey-Angle, K. L. 1993, PhD thesis, Utrecht University, Utrecht
- Higgs, L. A. 1962, *MNRAS*, 124, 51
- Keil, S. L., & Avakyan, S. 2003, *Innovative Telescopes and Instrumentation for Solar Astrophysics (Proceedings of the SPIE, Volume 4853)*
- Khomenko, E. V., Collados, M., Solanki, S. K., Lagg, A., & Trujillo-Bueno, J. 2003, *A&A*, 408, 1115
- Khomenko, E. V., Martínez González, M. J., Collados, M., Solanki, S. K., Ruiz Cobo, B., & Beck, C. 2005, *A&A*, 436, L27
- Kurucz, R. 1994, *Atomic Data for Fe and Ni*. Kurucz CD-ROM No. 22. Cambridge, Mass.: Smithsonian Astrophysical Observatory, 1994., 22
- Landi Degl'Innocenti, E. 1992, in *Solar Observations: Techniques and Interpretation*, ed. F. Sánchez, M. Collados, & M. Vázquez (Cambridge: Cambridge University Press), 71
- Lin, H., & Rimmele, T. 1999, *ApJ*, 514, 448
- Lites, B. W. 2002, *ApJ*, 573, 431
- Lites, B. W., & Socas-Navarro, H. 2004, *ApJ*, 613, 600
- Livingston, W. C., & Harvey, J. W. 1975, *BAAS*, 7, 346
- López Ariste, A., Rayrole, J., & Semel, M. 2000, *A&AS*, 142, 137

- Maltby, P., Avrett, E. H., Carlsson, M., Kjeldseth-Moe, O., Kurucz, R. L., & Loeser, R. 1986, *ApJ*, 306, 284
- Martínez Pillet, V., Collados, M., Sánchez Almeida, J., González, V., Cruz-Lopez, A., Manescau, A., Joven, E., Paez, E., Diaz, J. J., Feeney, O., Sánchez, V., Scharmer, G., & Soltau, D. 1999, in *ASP Conf. Ser.*, Vol. 183, *High Angular Resolution Solar Physics: Theory, Observations, and Techniques*, ed. T. Rimmele, K. S. Balasubramaniam, & R. Radick (San Francisco: ASP), 264
- Mein, P., & Rayrole, J. 1985, *Vistas in Astronomy*, 28, 567
- Moore, C. E., Minnaert, M. G. J., & Houtgast, J. 1966, *The Solar Spectrum from 2935 Å to 8770 Å*, NBS Mono. 61 (Washington: NBS)
- Nave, G., Johansson, S., Learner, R. C. M., Thorne, A. P., & Brault, J. W. 1994, *ApJS*, 94, 221
- Rast, M. P. 2003, *ApJ*, 597, 1200
- Rayrole, J., & Mein, P. 1993, in *ASP Conf. Ser. 46: IAU Colloq. 141: The Magnetic and Velocity Fields of Solar Active Regions*, 170
- Sánchez Almeida, J. 1997, *ApJ*, 491, 993
- Sánchez Almeida, J. 1998, in *ASP Conf. Ser.*, Vol. 155, *Three-Dimensional Structure of Solar Active Regions*, ed. C. E. Alissandrakis & B. Schmieder (San Francisco: ASP), 54
- Sánchez Almeida, J. 2003a, in *AIP Conf. Proc.*, Vol. 679, *Solar Wind 10*, ed. M. Velli, R. Bruno, & F. Malara (New York: AIP), 293
- . 2003b, *A&A*, 411, 615
- Sánchez Almeida, J., Domínguez Cerdeña, I., & Kneer, F. 2003a, *ApJ*, 597, L177
- Sánchez Almeida, J., Emonet, T., & Cattaneo, F. 2003b, *ApJ*, 585, 536
- Sánchez Almeida, J., Landi Degl'Innocenti, E., Martínez Pillet, V., & Lites, B. W. 1996, *ApJ*, 466, 537
- Sánchez Almeida, J., & Lites, B. W. 2000, *ApJ*, 532, 1215
- Sánchez Almeida, J., Márquez, I., Bonet, J. A., Domínguez Cerdeña, I., & Muller, R. 2004, *ApJ*, 609, L91
- Sánchez Almeida, J., & Trujillo Bueno, J. 1999, *ApJ*, 526, 1013
- Schlichenmaier, R., & Collados, M. 2002, *A&A*, 381, 668
- Schrijver, C. J., & Title, A. M. 2003, *ApJ*, 597, L165
- Schüssler, M. 1986, in *Small Scale Magnetic Flux Concentrations in the Solar Photosphere*, ed. W. Deinzer, M. Knölker, & H. H. Voigt (Göttingen: Vandenhoeck & Ruprecht), 103
- Sigwarth, M., Balasubramaniam, K. S., Knölker, M., & Schmidt, W. 1999, *A&A*, 349, 941
- Smithson, R. C. 1975, *BAAS*, 7, 346
- Socas-Navarro, H., Elmore, D., Pietarila, A., Darnell, A., Lites, B. W., & Tomczyk, S. 2005, *Sol. Phys.*, in press, astro-ph/0508685
- Socas-Navarro, H., Martínez Pillet, V., & Lites, B. W. 2004, *ApJ*, 611, 1139
- Socas-Navarro, H., & Sánchez Almeida, J. 2002, *ApJ*, 565, 1323
- . 2003, *ApJ*, 593, 581
- Solanki, S. K. 1986, *A&A*, 168, 311
- Solanki, S. K., & Stenflo, J. O. 1986, *A&A*, 170, 120
- Stein, R. F., & Nordlund, Å. 2002, in *IAU Colloquium 188*, ed. H. Sawaya-Lacoste, ESA SP-505 (Noordwijk: ESA Publications Division), 83
- Stenflo, J. O. 1982, *Sol. Phys.*, 80, 209
- Trujillo Bueno, J., Shchukina, N. G., & Asensio Ramos, A. 2004, *Nature*, 430, 326
- Unno, W. 1959, *ApJ*, 129, 375
- Vögler, A. 2003, PhD thesis, Göttingen University, Göttingen
- Vögler, A., & Schüssler, M. 2003, *Astron. Nachr.*, 324, 399
- Vögler, A., Shelyag, S., Schüssler, M., Cattaneo, F., Emonet, T., & Linde, T. 2005, *A&A*, 429, 335
- Zhang, J., Lin, G., Wang, J., Wang, H., & Zirin, H. 1998, *Sol. Phys.*, 178, 245